Title

Trace Fe activates perovskite nickelate OER catalysts in alkaline media via redox-active surface Ni species formed during electrocatalysis

Authors

Twight, Liam
Tonsberg, Ally
Samira, Samji
et al.

Publication Date

2024-04-01

DOI

10.1016/j.jcat.2024.115443

Peer reviewed

Trace Fe in alkaline electrolyte governs the OER activity of perovskite $LaNiO_3$ and La_2NiO_4 via interaction with redox-active surface NiO_xH_y formed by applied bias.

Liam Twight[1], Ally Tonsberg[1], Samji Samira[2,3], Kunal Velinkar[3,4], Kora Dumpert[1], Yingqing Ou[1,5] , Le Wang[6], Eranda Nikolla[3,4], and Shannon Boettcher[1*].

[1] Department of Chemistry and Biochemistry and the Oregon Center for Electrochemistry, University of Oregon, Eugene, Oregon 97403, United States

[2] Department of Chemical Engineering, University of California Santa Barbara, Santa Barbara, California, 93106, United States

[3] Department of Chemical Engineering and Materials Science, Wayne State University, Detroit, Michigan 48202, United States

[4] Department of Chemical Engineering, University of Michigan, Ann Arbor, Michigan 48109, United States

[5] School of Chemistry and Chemical Engineering, Chongqing University, Chongqing 400044, China

[6] Physical and Computational Sciences Directorate, Pacific Northwest National Laboratory, Richland, WA, 99354 USA

e-mail:

* Shannon W. Boettcher: swb@uoregon.edu

Abstract

Accurate description of activity trends among perovskite oxide oxygen evolution catalysts using electronic descriptors requires that the bulk structure of the catalyst is comparable to that of the surface. Few studies have thus far addressed the dynamic nature of the catalyst's structure during the oxygen evolution reaction (OER) and the consequential implications for rationalization of activity. Here, we use a combination of electrochemical and materials characterization techniques to show the surface reconstruction of $LaNiO_3$ particles, $LaNiO_3$ epitaxial films, and an analogous Ruddlesden-Popper phase, La_2NiO_4. Small, but characteristic redox features corresponding to Ni redox in amorphous NiO_xH_y are observed during cyclic voltammetry of these nominally crystalline materials. The size of these redox features grows with prolonged cycling and contributes to an increased surface area as determined from electrochemical impedance

spectroscopy (EIS). These observations are consistent with the reconstruction of the crystalline surface into NiO_xH_y and subsequent activation by adsorption of Fe forming the well-known and extremely active $NiFeO_xH_y$ OER catalyst.

Introduction

Perovskite oxides have been studied as oxygen evolution reaction (OER) catalysts for decades due to their high activity and use of relatively abundant transition metals[1]. Early reports to rationalize the activity of these catalysts made use of activity correlations with bulk thermodynamic concepts such as lower to higher enthalpy of oxidation and d-electron count on the B-site metal cation[2]. More recently, descriptors such as the extent of transition metal-oxygen hybridization (covalency)[3], O-2*p* band position band position relative to the Fermi energy[4], and e_g electron count of the transition metal cation[5] have been used to connect the activity of perovskite oxides to their electronic structures.

Bulk electronic structure descriptors can be useful for developing a physical and possibly predictive model for perovskite OER activity, as has been done for the hydrogen evolution reaction (HER) on metal surfaces[6-8]. However, the predictive power of these descriptors can be limited by dynamic processes that occur on the surface of perovskite oxides, causing large deviations of surface chemistry from that of the bulk. In such a case, electronic descriptors of the bulk may fail to accurately capture the relevant mechanistic parameters *of the active surface*. The most dramatic examples of dynamic surface phenomena among perovskites involves those with partial substitution of alkaline-soluble species, like Sr^{2+}, at the A-site. $Ba_{0.5}Sr_{0.5}Co_{0.8}Fe_{0.2}O_3$ (BSCF), was proposed to be extremely active based on its optimal e_g electron count of around unity[5], but was later found to be unstable during OER[9]. Large proportions of the surface and eventually parts of the bulk amorphized via Sr-leaching and oxygen-vacancy formation forming an highly OER active $Co(Fe)O_xH_y$ surface phase,[9] similar to that made by other methods such as electrodeposition[10]. In a related study, a surface Co/Fe spinel oxide minority species on the underlying BSCF perovskite was determined to be responsible for dynamic, reversible conversion to an oxyhydroxide[11]. The implication of these studies is that prior rationalization of high activity based on bulk electronics of the pristine BSCF alone failed to capture the real properties of the surface-active phase which has different oxidation states, composition, protonation state, and local structure – the active surface phase is in this case a completely different material.

Markovic and coworkers showed that in a series of $La_{1-x}Sr_xCoO_3$ compounds, surface reconstruction to amorphous CoOOH was observed following Sr dissolution and oxygen-vacancy formation measured with on-line inductively-coupled-plasma mass spectroscopy (ICP-MS) and identical-location transmission electron microscopy (IL-TEM) analyses. They further showed that this amorphous

Co phase was activated by trace Fe impurities in the electrolyte, forming dynamically stable active sites[12]. Boucly *et al.* found that the deposition temperature during pulsed epitaxial growth of $La_{1-x}Sr_xCoO_3$ led to different extents of soluble Sr species (hydroxides, carbonates, and/or oxides) which dissolve upon immersion of water, leaving a Co-rich surface layer. Higher extent of Sr dissolution and surface Co exposure correlated with higher OER activity[13]. In a follow-up to this work, it was shown that not only Co-richness at the surface, but *reconstruction of the Co* formed by Sr dissolution to CoO_xH_y was the source of OER activity from $La_{0.2}Sr_{0.8}CoO_3$.[14] The intrinsic activity of the parent perovskite oxide with the pristine surface termination remains an open question – the presence of disordered conformationally dynamic surface phases with low activation barriers to rearrangement during the water oxidation process in fact may be key to driving water oxidation at any reasonable overpotential.

Amorphous Co hydroxides, such as those observed on certain perovskites after OER, are active catalysts[15], especially in the presence of Fe impurities[16]. Compared to Co-based perovskites, investigation of dynamic surface processes and interaction of secondary phases formed by these processes with Fe impurities on Ni-based perovskites is relatively less understood. Moreover, identifying and characterizing the structure and activity of reconstructed Ni phases in the presence of Fe may be even more important than for Co-based systems because the activation of NiO_xH_y by Fe is even more pronounced than for CoO_xH_y[17].

In this report, we present evidence of surface reconstruction of $LaNiO_3$ (LNO) particles to nominally NiO_xH_y. This phenomenon is supported by the observation of electrochemical redox features typically attributed to NiO_xH_y present in the voltammetry of nominally crystalline LNO. These features become more pronounced with extended cycling and constant-current conditioning of the catalyst. We further show the activation of LNO by trace Fe impurities intentionally introduced in an otherwise Fe-free electrolyte. Adsorption of intentionally added Fe onto the catalyst surface leads to an approximate doubling of the OER activity, despite the trace amounts of both Fe and reconstructed surface Ni phase. Estimated turn-over frequencies for the proposed surface-active formed Ni(Fe)OOH active phase are consistent with known high activities of as-synthesized hydroxides. These new insights have significant implications for past and future studies of apparent intrinsic activity of the large class of perovskite-oxide OER catalysts.

Results and Discussion

Redox active Ni is apparent from cycling and grows with cycle number. To investigate the structural stability of LNO during OER, the catalyst was first cycled 100 times between 0 and 0.8 V vs Hg|HgO (0.9 – 1.7 V vs RHE) in 0.1 M KOH at a scan rate of 20 mV s^{-1}. We hypothesized that if LNO is thermodynamically unstable during OER, as has been posited as a universal feature of oxides[18], restructuring to the stable NiO_xH_y phase would occur at the LNO surface on a timescale dictated by the oxide transformation kinetics. Such a structural change may be evident in observable loss of crystalline

phase purity, emergence of redox features, and/or an increased double-layer capacitance, depending on rate and extent. Figure 1a shows the evolution of current response within the cyclic voltammogram. The measurements were conducted in purified, Fe-free 0.1 M KOH solution using an LNO film made by dropcasting 10 µL of a 26.2 µg/µL ink which has a 5:1:1 mass ratio LNO, acetylene carbon black, and Nafion (neutralized), respectively. Phase purity of the LNO catalyst was confirmed by powder X-ray diffraction (Supplementary Figure 1). Within two cycles, pre-catalytic redox waves emerged, with the anodic wave positioned at ~1.32 V vs the reversible hydrogen electrode (RHE) (0.49 V vs Hg/HgO). This feature remained throughout continued cycling and its integrated area increases by ~4-fold after 100 cycles. The corresponding amount of Ni assuming a 1 e^- oxidation is given in Fig 1b for selected cycles. The redox feature peak positions agree well with the known Ni^{2+}/Ni^{3+} redox process of amorphous nickel (oxy)hydroxides[19-21]. A potential mechanism for growth of the secondary NiO_xH_y phase on the catalyst surface could involve dissolution and redeposition of Ni cations from the oxide surface during OER. Alternatively, the surface could undergo a voltage driven, direct solid-solid phase transition as the surface cations change oxidation state and coordinate with water and hydroxide. However, further research is needed to comprehensively understand the descriptors that govern the actual operative mechanism.

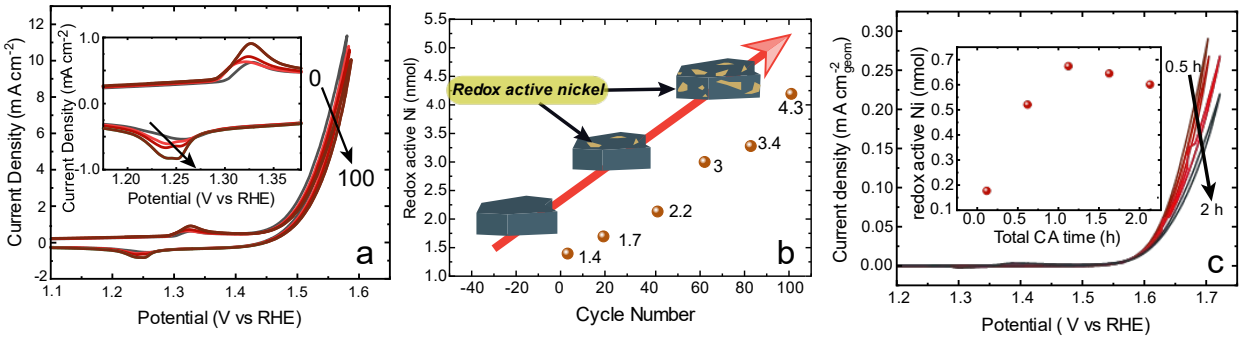

Figure 1. a) 100 CV curves of $LaNiO_3$ in rigorously Fe-free 0.1 M KOH electrolyte at room temperature. Inset clearly shows the evolution of Ni redox feature with cycling. **b)** Secondary Ni phase redox features grow in size up to about 4 nmol. **c)** CV curves taken at 30 minute intervals during a 2 hour chronoamperometry of LNO in Fe-free conditions. and the similar increase in redox peak area size with charge passed in OER (inset).

To understand if the redox-active changes in the Ni surface structure only stem from a cyclic application of voltage, we also performed chronoamperometric studies. It was found that redox-active Ni growth was not dependent on the cyclical application of voltage. Chronoamperometry (CA) at 0.8 V vs Hg/HgO of a spincoated film was performed over 2 h with diagnostic CVs scanned at a rate of 20 mV s^{-1}

taken before the experiment and at 30-minute intervals (Fig 1c). Integration of redox waves show that the amount of NiO_xH_y increases over the first hour, then plateaus and drops slightly over the second hour. Immersion of a pristine electrode in 1 M KOH was done to test if chemical reconstruction occurs simultaneously with electrochemical reconstruction. No change in the redox wave size occurred from immersion alone (Supplementary Figure 7). Application of anodic voltage was *required* for this Ni redox feature to increase. That the redox wave size appears to plateau via CA rather than gradually increasing in size during CVs suggests that the expansion and contraction of bond lengths which accompanies voltage cycling can prolong reconstruction relative to CA, perhaps by accessing more tightly coordinated subsurface Ni. The slight loss of activity over the experiment duration (Figure 1c) suggests that this as-grown secondary phase is less active than the underlying LNO catalyst, although this could also be due to the insulation of active material by bubble formation. Additional work describing precisely how applied potential affects redox active Ni formation is still needed.

X-ray photoelectron spectroscopy (XPS) was used to detect the formation of new surface Ni phases on LNO electrodes after extended cycling. The XPS spectra of the most intense lines – Ni 2*p* and La 3*d* – are difficult to interpret and deconvolute. Both Ni 2*p* and La 3*d* have multiplet structure and accompanying satellites[22,23,24] which directly interfere with each other. Consequently, little information was gleaned from these regions. Therefore, we restrict our interpretation to the O 1*s* region where large, reproducible changes were observed. Figure 2 shows the comparison of O 1*s* XPS for LNO before and after 100 cycles. After cycling, a significant decrease in the characteristic lattice oxygen feature located at ~528 eV was observed and the O 1*s* XPS core level spectra resembles that of pure $Ni(OH)_2$[25,26]. The peak at higher binding energies, associated with weakly adsorbed oxygenated species and oxidized carbon, may also increase due to oxidation of the ionomer binder[27] and/or surface hydroxylation after exposure to alkaline electrolyte. Given the signs of reconstruction in the cyclic voltammetry, we assign the loss of the lattice oxygen feature to a decrease in crystalline oxide-like structure at the catalyst surface after cycling from transformation to NiO_xH_y. The disappearance of the ~528 eV

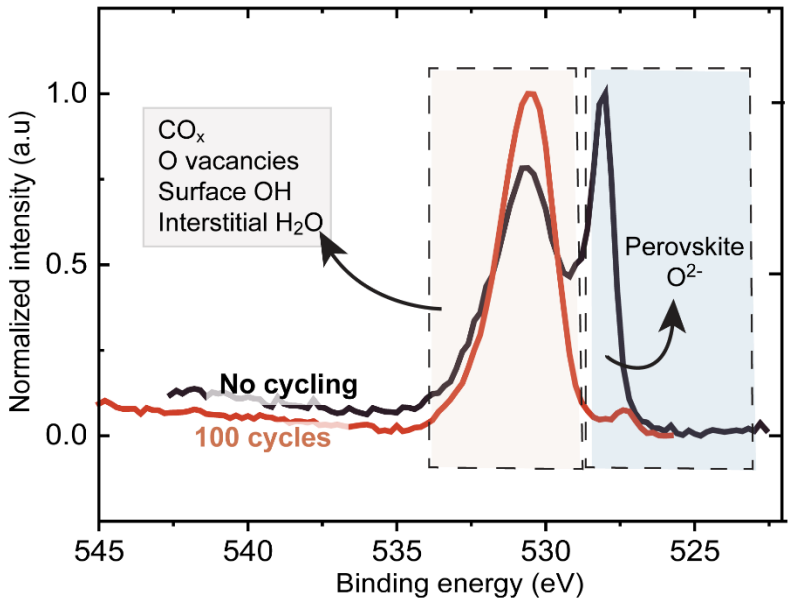

Figure 2. O-1*s* XPS spectra of LNO before and after 100 cycles in 0.1 M KOH.

component within the O 1*s* spectra of initially crystalline nickel-based oxides upon electrochemical conditioning is not without precedent and has been shown to correspond to conversion of NiO to $Ni(OH)_2$[19]. However, the decrease in intensity in the low binding energy region might also arise from formation of a layer containing weakly adsorbed species which attenuates the signal originating from the underlying crystalline O^{2-}. A layer of weakly adsorbed species would likely be thinner than the XPS penetration depth so likely cannot account for the large changes in the O 1*s* spectra. Direct identification of NiO_xH_y presence is not possible from the oxygen scan because it is located at >530 eV[25].

Growth of an (oxy)hydroxide layer may lead to an increase in the electrochemically active surface area. This can be probed from the double-layer capacitance (C_{dl}) obtained via electrochemical impedance spectroscopy (EIS)[28]. Impedance scans taken every 25 cycles up to 75 cycles of LNO are shown in Figure 3. Note that EIS was measured with the DC potential in the OER region (~1.7 V vs RHE; 0.8 V vs Hg|HgO) rather than at open circuit because NiO_xH_y is only conductive at OER potentials[28]. C_{dl} measured in the non-faradaic open-circuit region is representative only of the conductive support, not the active surface phase. C_{dl} increased with prolonged cycling and the data directly mirror the increasing redox-active Ni from integrating the pre-OER redox wave. This result is consistent with the observed increase in surface area being due to the changing amount of Ni redox species at the LNO surface. Assuming that the change in C_{dl} every 25 cycles is due to the redox-active Ni phase, we can calculate the amount of Ni contributing to that change using the capacitance per monolayer equivalent of NiOOH established from previous work[28]. Comparing this value to the change in redox peak area, we find the two values are in good agreement (Supplementary Figure 9). Consistency between the amount of Ni from the redox wave and that predicted from EIS using NiOOH as a model[28] further suggests that the Ni redox from LNO can be assigned to a (oxy)hydroxide-like phase. Decreasing charge transfer resistance may be from the incorporation of trace Fe in this experiment, which would also explain the slight improvement of activity during cycling in this experiment. We note that Fe was not measured explicitly here, and the role in activation by Fe impurities is discussed below.

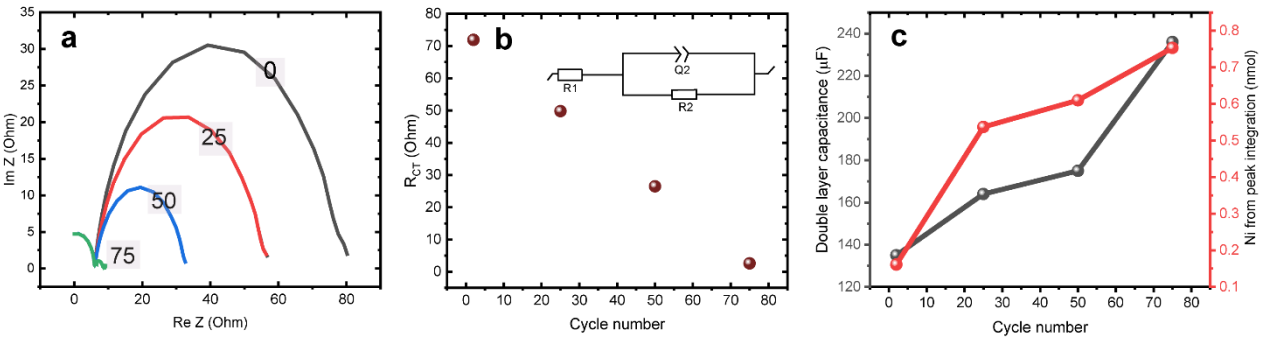

Figure 3. a) EIS of LNO at ~1.7 V vs RHE after 0, 25, 50, and 75 cycles in 1 M KOH showing **(b)** decreasing R_{CT} as a function of cycle number. Inset shows equivalent circuit used to fit the data: solution and cell resistance, R1, in series with a Randles cell element with constant phase element Q2 parallel with faradaic impedance, R2. **c)** Double-layer capacitance (C_{dl}) and Ni from redox peak integrated area as a function of cycle number

$LaNiO_3$, La_2NiO_4, and epitaxial $LaNiO_3$ thin films are all activated by electrolyte Fe impurities.

After cycling, if the surface phase on LNO is nominally NiO_xH_y, the introduction of trace Fe impurities into rigorously Fe-free KOH electrolyte should increase OER activity via the formation of $NiFeO_xH_y$[29]. In fact, we do observe enhanced OER activity for LNO for particles (Figure 4a) and epitaxial films (Figure 4c) upon introducing 100 ppb Fe^{3+} into the KOH solution by spiking from an $Fe(NO_3)_3$•$9H_2O$. Besides LNO, we observed similar effects for Ruddlesden-Popper rod-shaped La_2NiO_4 (Figure 4b). For the LNO particles, the OER activity slightly decreases after the first cycle, then stabilizes, resulting in comparable activity in 15th through 106th cycle in Fe-free electrolyte. After cycle 106, 100 ppb of Fe was spiked into the electrolyte. Initially, a slight increase in the current was observed in cycle 107 and then dramatically in subsequent cycles leading to a ~5-fold improvement by cycle 112. A large increase in current occurs within 4-5 cycles after spiking, after which the improvement continues, but at a slower rate. The different rate of activity enhancement in earlier cycles compared to later ones is attributed to initial rapid Fe adsorption to redox-active NiO_xH_y formed before the spike, making high-activity $Ni(Fe)O_xH_y$. In subsequent cycles, the current increases more slowly because all sites for Fe adsorption have been filled and formation of more high activity Fe sites is bottlenecked by the incremental increase in reconstructed Ni every cycle. In a typical Fe-spiking experiment with electrodeposited NiO_xH_y, Fe adsorbs to surface sites immediately after spiking which increases the OER activity greatly, but only marginally increases with further cycling[29]. The Ni peak position also shifts anodically ~30 mV with 100 cycles in Fe-spiked conditions indicating electronic mixing by Fe incorporation into bulk Ni sites.[29, 30]. Using this result from Stevens *et al.* we would expect an anodic shift of about 4 mV over 14 cycles (30 mV/100 cycles = 0.3 mV cycle^{-1}) if the redox-active Ni on LNO resembles NiO_xH_y. Interestingly, the peak position after spiking indeed shifts, ~4 mV total. Rod-shaped La_2NiO_4 nanostructures (214-LNO) and epitaxial LNO also exhibit the same general change in OER activity after Fe-spiking. It is worth highlighting that since the increase in

OER activity by introduction of Fe is a shared trait among these oxides, it can be used as a convenient indicator to determine whether the materials reconstruct, a strategy that has been highlighted recently in the $Li_xCo_{1-x}O_4$ family of materials[31]. Interestingly, we find that $LaCoO_3$ exhibits no such Fe activation (Supplementary Figure 6) which suggests its surface is more stable and does not as easily form cobalt-oxyhydroxide-like surface-phases consistent with previous literature[32]. Given that these materials are isostructural (and $LaCoO_3$ are rhombohedral belonging to $R\bar{3}c$ space group)[33], we hypothesize that the enhanced stability with respect to surface-phase reconstruction arises from stronger Co-O bonding compared to Ni-O[34]. This is also consistent with the higher surface reduction temperature as observed from H_2-temperature programmed reduction studies which indicate stronger Co-O bonding in $LaCoO_3$, as compared to Ni-O bonding in $LaNiO_3$.[33]

If we assume the observed Ni-based redox to originate from the (oxy)hydroxide-like structure, we can then integrate the redox peak areas in Figure 4 to calculate number of monolayer equivalents (MLE) of $Ni(OH)_2$ formed at the surface. We estimate ~1.7 nmol Ni cm^{-2} for a single MLE based on the unit cell parameters for brucite β-$Ni(OH)_2$ (International Crystal Structure Database structure code: 169978), as discussed by Batchellor *et al.*[28]. We find that the 214-LNO has 2.4 ± 0.6 MLE and LNO has 0.3 ± 0.1 MLE of nominally $Ni(OH)_2$ after 30 cycles. If the entire catalytic surface reconstructs homogeneously (does not form isolated pockets), this suggests that there is multiple monolayers of Ni(Fe)OOH present on nickelates given sufficient time of electrochemical treatment and trace Fe in the electrolyte.

The magnitude of the enhancement observed in the first cycle immediately after Fe-spiking was variable, implying that the Fe-activation process is controlled by a mix of factors such as mass transport and accessibility of adsorption sites. Extended cycling (>100 CVs) is not necessary to observe an increase of activity after Fe spiking. Fe-based activity enhancement reproducibly occurs in as few as 8 cycles and with only 30 ppb of Fe^{3+} in the electrolyte, an amount below the solubility limit of Fe^{3+} in 1 M KOH[35] (Supplementary Figure 8). The latter observation aligns with activation from the uptake of soluble Fe and not from adsorption of FeOOH precipitate or colloids, although these may be relevant at higher Fe concentrations. Ni redox waves cannot be attributed the adsorption of $Ni(OH)_2$ particulates, that might persist from using our $Ni(OH)_2$-based Fe sorbent during electrolyte purification. Supplementary Figure 4 shows that when the purification is performed with $Co(OH)_2$, Ni redox peaks are still observed as usual. Previous work has also verified that the use of a 0.1 um PES filter, as used here, is sufficient to remove $Ni(OH)_2$ particulates from 1 M KOH electrolyte[36] when using $Ni(OH)_2$ as an Fe sorbent.

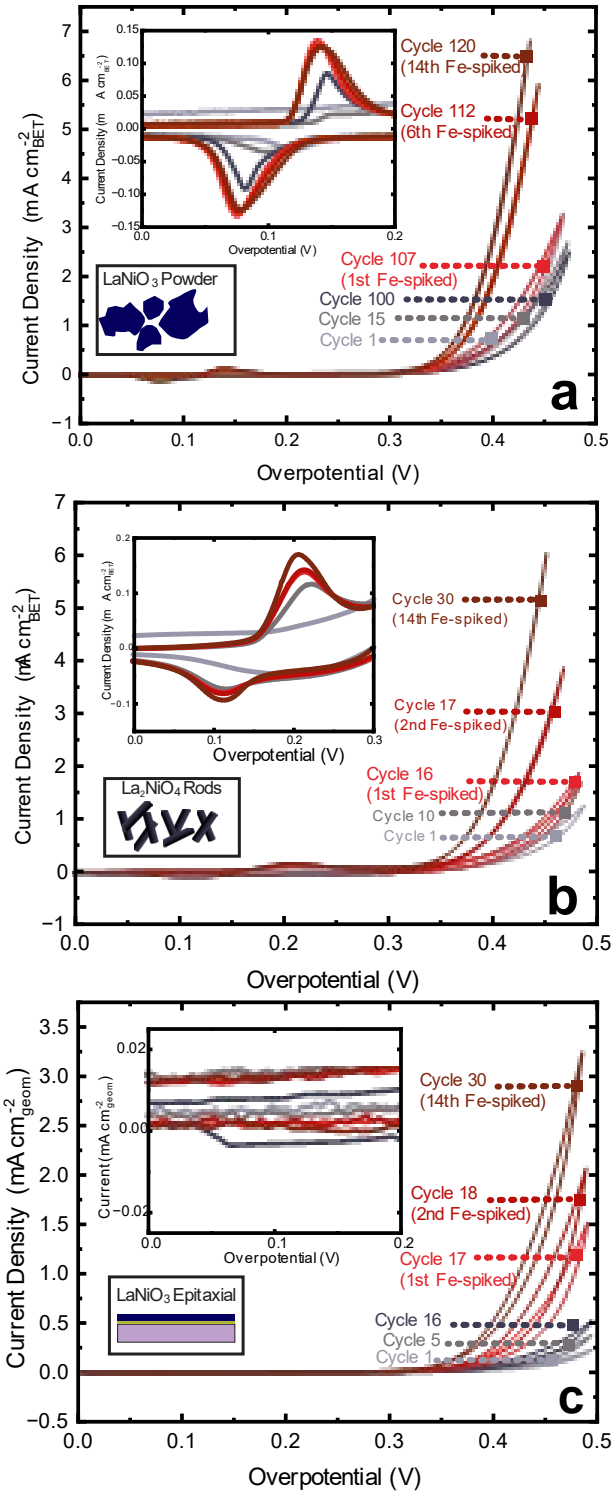

Figure 4. Comparison of activation of **(a)** particulate $LaNiO_3$, **(b)** La_2NiO_4 nanorods, and **(c)** epitaxial $LaNiO_3$ films upon introduction of 100 ppb $Fe(NO_3)_3$ into Fe-free 1.0 M KOH electrolyte at room temperature. Gray curves indicate Fe-free conditions and red curves indicate Fe-spiked conditions. Inset CVs highlight the region of Ni redox wave evolution at each cycle.

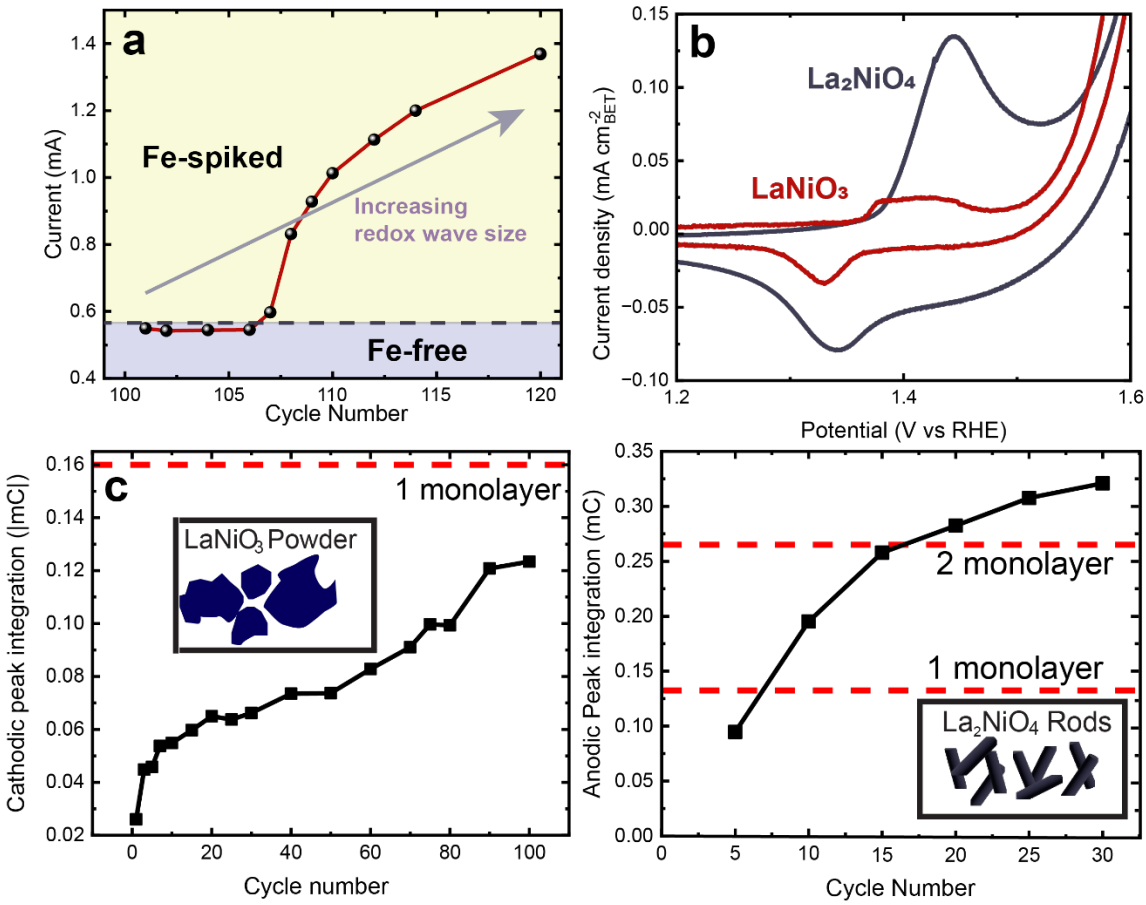

Figure 5. (a) Relationship between cycle number and current during a typical Fe-spiking experiment with $LaNiO_3$ and **(b)** comparison of the redox-wave size between $LaNiO_3$ and La_2NiO_4 for the 15th Fe-free cycle. Panels **(c)** and **(d)** show the cathodic peak area charge for a given cycle for $LaNiO_3$ powders and La_2NiO_4 nanorods, respectively. The inset red, dashed lines correspond to the threshold beyond which there is enough redox-active $Ni(OH)_2$ to cover the perovskite sample in the given number of monolayers. The data chosen shows the reproducible fact that La_2NiO_4 has more redox active Ni and larger possible monolayer coverage at a given cycle number on a per area basis. Potentials are iR_u-compensated

Investigation of the La_2NiO_4 nanorods (214-LNO) may yield insight into the reasons behind surface reconstruction and Fe activation by comparison to $LaNiO_3$. The rod-shaped geometry of 214-LNO as well as its tetragonal structure corresponding to the I4/*mmm* space group was confirmed using TEM imaging and X-ray diffraction (XRD) studies, respectively (Supplementary Figure 10). Previous TEM and selected-area electron-diffraction (SAED) experiments show that the nanorods are primarily terminated by (001) facets along their longitudinal axis[37]. Depth-profiling low-energy ion-scattering spectroscopy (LEIS), atomic-resolution high-angle annular dark-field (HAADF) imaging, and electron energy loss spectroscopy (EELS) performed in aberration-corrected scanning TEM (STEM) mode revealed that the (001) facets were

primarily Ni-O terminated rather than La-O terminated[38, 39]. Figure 5b shows the 15th Fe-free CV curves for an LNO and 214-LNO electrode. On a Brunauer-Emmett-Teller (BET) surface area-normalized basis, the redox wave size is larger for 214-LNO. This phenomenon is potentially attributed to the rapid restructuring pathways provided by the Ni rich (001) surfaces of the nanorod bodies. Notably, the redox peak positions for both materials are closer to those observed in ordered β-$Ni(OH)_2$ than in disordered α-$Ni(OH)_2$. This could stem from the influence of the crystalline LNO substrate on the *in-situ* grown Ni surface phase, leading to higher structural order. Such influence of the substrate structure on a grown overlayer is reminiscent of strain-induced electronic structure changes in epitaxial $LaNiO_3$ films[40]. The high proportion of Ni-terminated surface in the 214-LNO material could explain the faster rate of reconstruction of the first monolayer surface, but the apparent ease with which subsurface monolayers of NiO_xH_y form on 214-LNO suggest that the bulk chemical differences are also important. We hypothesize that oxygen nonstoichiometry and transport play critical roles, especially considering that the electrochemical dissolution inherently involves the formation of oxygen vacancies[18]. Since $LaNiO_3$ powders studied here were not prepared in a pure O_2 atmosphere, they are *sub*stoiochiometric in term of oxygen. By contrast, La_2NiO_4 is known to possess oxygen *super*stoichiometry[41]. Further study is needed to understand how the concentration and formation energy of oxygen vacancies at the surface and bulk of these materials influences the restructuring process, if at all.

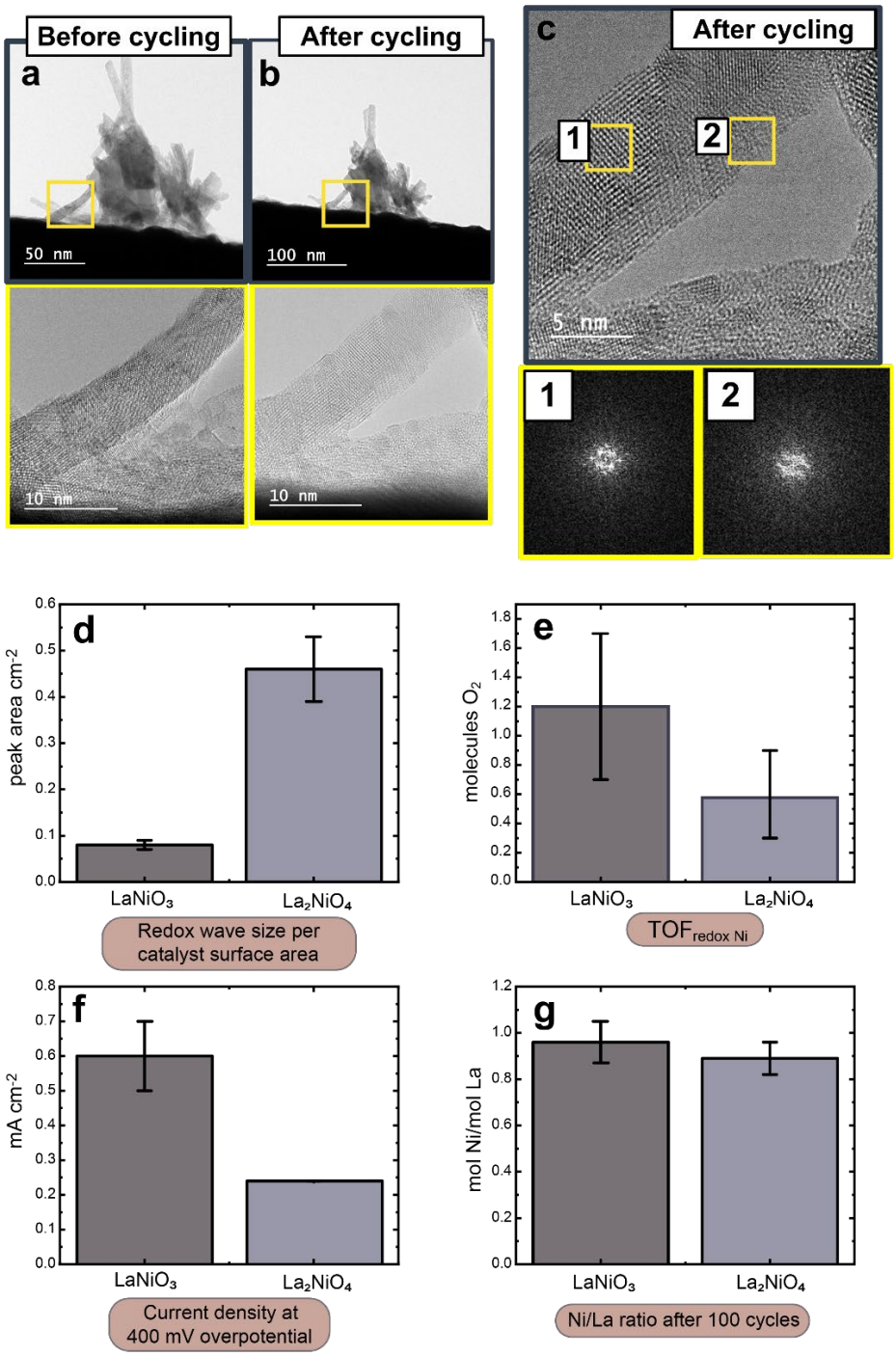

Figure 6. (a-c) IL-TEM studies of La_2NiO_4 nanorods before and after 300 cycles with corresponding FFTs. **(d)** shows the intrinsic tendency toward redox active Ni formation, **(e)** TOF of Fe-based active sites formed after Fe-spiking, **(f)** the intrinsic Fe-free activity of each catalyst at 400 mV overpotential, and **(g)** the Ni:La stoichiometry after 100 cycles from ICP-MS measurements.

Identical location TEM (IL-TEM) was conducted on the LNO particulate materials before and after cycling with the aim of observing any obvious signs of structural changes such as amorphization. No clear surface layers were observed, likely because of the near-atomic thinness of any reconstructed layers, illustrating the central role of electrochemical techniques in understanding surface transformations. The larger per surface-area growth of redox-active Ni on 214-LNO would increase the likelihood of observing structural changes. Figures 6a-c show the near-surface structure of a cluster of nanorods before (6a) and after (6b-c) 300 cycles in 1 M KOH. The apparently identical appearance of the cluster indicates that the same area and particles were successfully imaged both before and after cycling. We observed regions which apparently lack the crystalline order of neighboring areas after cycling as can be seen by the fast Fourier transform (FFT). This is a cautious interpretation because TEM studies can be subject to a variety of imaging artefacts and over-interpretation. Further experiments with an epitaxial model system, grazing-angle X-ray techniques, and detailed X-ray absorption fine structure experiments are needed to understand the precise connection between Ni redox and surface structure.

In order to develop a better understanding of the changes in the composition, inductively-coupled plasma mass spectroscopy (ICP-MS) studies of the oxide electrode were performed (Figure 6g). The pre-OER Ni:La ratio of 1:2 for 214-LNO was measured to be ~ 1:1.1 after 30 cycles, indicating a loss of La and an increase in Ni. In contrast, the stoichiometry of $LaNiO_3$ did not change from the as-prepared 1:1 ratio within the error of our measurements. The more pronounced A-site leaching observed in 214-LNO may be related to the structural differences between the perovskite and Ruddlesden-Popper phases. The La-O rock salt layers in the latter may be more unstable to dissolution than the perovskite La-O regions. We note that the ICP-MS results in another study found negligible La dissolution in the Sr-doped version[42] possibly because the introduction of Sr^{2+} increased the valence of Ni and therefore the Ni-O bond strength. Figure 6d underscores the higher tendency for La_2NiO_4 to generate redox-active Ni as evidenced by a peak area per BET surface area which is ~5-fold larger compared to $LaNiO_3$ after 15 Fe-free CVs. This is consistent with the structural change observed by TEM and the large composition change. Redox features have been previously observed in cyclic voltammograms on $La_{0.5}Sr_{1.5}NiO_4$[42] and $La_{0.5}Sr_{1.5}Ni_{1-x}Fe_xO_{4+\delta}$[43]. The latter study[43] also reported a positive voltage shift of the Ni redox positions with increasing Fe substitution consistent with the growth of a NiFeOOH phase as proposed here. However, the authors did not find significant amorphization (no post-mortem surface images were provided). Therefore, to our knowledge, this is the first report connecting *in-situ* redox active Ni to Fe impurities in promoting OER catalysis.

We next further calculated the intrinsic activity of the various hypothesized Fe-Ni active sites to compare across the different systems—if the intrinsic activities per metal ion are similar, then their surface-

active species are likely also similar in nature. A total-redox metal turnover frequency ($TOF_{tm,redox}$) was calculated by taking the number of redox-active Ni as the site density and the current jump Δi (400 mV overpotential) between Fe-free and Fe-spiked measurements as the catalytic current associated with the Ni-O-Fe proposed active sites formed under operating conditions:

$$\mathrm{TOF_{tm}}(s^{-1}) = \frac{\Delta i}{4F(n_{\mathrm{redox\ Ni}})} \quad (1)$$

The term $n_{\mathrm{redox\ Ni}}$ is the moles of Ni obtained from the redox wave of the last Fe-free cycle plus 25% Fe incorporation which is the reported estimated solubility of Fe in NiOOH[44]. The amount of Fe adsorbed was obtained with ICP-MS, but this value would be an overestimate as it includes adsorbed Fe on the Pt substrate and binder so was not used. Since the amount of spiked Fe was always well in excess of what can be maximally absorbed by NiOOH, 25 at. % (with respect to Ni) incorporation was assumed. Figure 6e shows the value of $TOF_{tm,redox}$ for replicate analyses of $LaNiO_3$ and La_2NiO_4. Within error, the intrinsic activity of the Fe-based active sites formed by spiking are the same. Therefore, despite difference in initial structure, the *in-situ* formed Ni species appears to have the same catalytic activity, consistent with the idea that the application of potential drives the transformation of Ni toward the same phase that is most thermodynamically stable under OER conditions.

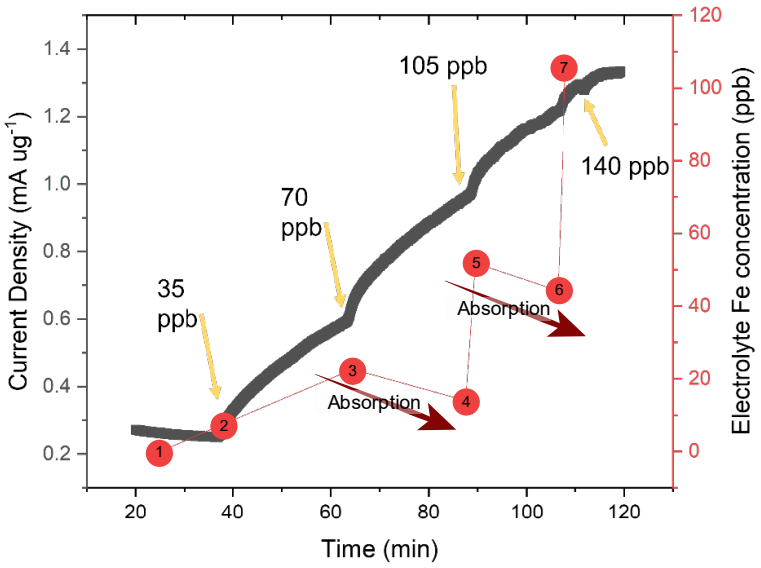

Figure 7. Chronoamperometry with intermittent Fe-spikes reported as mass activity versus time. Yellow arrows show points where a replicate additional Fe spike was performed. Concentration labels (black text) are the nominal Fe concentration at the time of the spike. Numbered circles indicate actual concentration of Fe (red axis) in the electrolyte measured from ICP-MS.

Activation of the reconstructed NiO_xH_y after spiking a small amount of Fe into 1.0 M KOH was evident in the cyclic voltammograms. It was not clear if this enhancement was sustained during constant voltage application nor whether successive additions of Fe promoted further activity enhancement. Figure 4 shows 2 h of chronoamperometry at 1.7 V vs RHE on a LNO electrode with additions of Fe at regular intervals. The yellow arrows indicate the approximate time and nominal concentration of electrolyte Fe after the spike while the red squares show the actual concentration of Fe in an aliquot of the electrolyte which was later measured by ICP-MS. The concentration of Fe in the electrolyte before the experiment was below the detection limit of ^{57}Fe in our ICP-MS of 3.9 ppb. Points 2, 3, 5, and 7 are aliquots of the electrolyte taken immediately after (~10-20 s) successive spikes of Fe. Points 4 and 6 are aliquots withdrawn before the corresponding spikes. Note that between the 2nd and 3rd, and 3rd and 4th spikes, the Fe concentration in the electrolyte decreases while the activity increases. This observation provides direct evidence that Fe adsorption from the electrolyte onto the electrode correlates with higher OER activity. Moreover, the impact of Fe adsorption on activity is noticeable even without performing any cyclic voltammetry, an observation which emphasizes that Tafel slopes and other activity parameters from chronoamperometric data must be collected in purified electrolyte for these materials to avoid effects of Fe-activation. After 2 h the activity appears to plateau, possibly because the extent of surface reconstruction by chronoamperometry has reached its maximum and no further $NiFeO_xH_y$ can be formed (as shown in Figure 1)

Redox features, like those we assign to surface (oxy)hydroxide phases, are often found in voltammetry studies on crystalline OER catalysts like perovskite oxides. Yet there has been little discussion about their possible origin, their effect on measured OER activity, and their ability to report on the interaction with soluble Fe [45-47]. Recently, however, epitaxial films have been studied as a model to understand the chemical drivers of this restructuring. Baeumer et al observed large redox features in the pre-OER region when cycling single-crystal epitaxial $LaNiO_3$ films which they assigned to a "nickel-oxyhydroxide-like" surface layer that lowered the overpotential for OER by 150 mV. They found that this transformation occurs on Ni-terminated films with the size of the redox feature decreasing monotonically with increasing surface La termination. Optical experiments further supported the transformation of the Ni-terminated surface to an oxyhydroxide[48]. Localized amorphization on $LaNiO_3$ epitaxial films has also been directly observed with TEM in another study, but the possible role of these regions in OER was not discussed[49]. In another example, perturbation of the surface oxygen octahedra was observed via TEM when Fe was "exchanged" from electrolyte to thin films of $LnNiO_3$ (Ln = Ln, Nd, Pr. These authors did not invoke the concept of a NiFeOOH surface layer[50], rather, they suggested that Fe^{3+} substituted for Ni sites in the perovskite structure. Nonetheless, their observations hinted at possible structural changes induced by Fe interactions. Additionally, Adiga and coworkers investigated a series of $La_{0.5}Sr_{0.5}Ni_{1-z}Fe_zO_3$ ($z = 0 – 0.5$) epitaxial thin films and found that the top roughly two unit cells of these materials showed amorphization

and Sr-leaching after 15 cycles. A decrease in the oxide feature was observed in their post-cycling XPS scans[51] similar to our observations.

The results presented in this study adds a class of materials, perovskite and Ruddlesden-Popper oxide nickelates, to the growing roster of pre-catalysts where Fe impurities, whether introduced intentionally or not, play an important role in boosting OER activity. The role of Fe has already been well established among pure electrodeposited NiO_xH_y,[20, 52, 53] Ni-based chalcogenides,[54, 55] and CoO_xH_y[56]. A common theme emerging from these diverse materials is amorphization of A-site doped perovskite oxides, leading to the formation of active Fe-containing surface phases that are the actual agents responsible for catalysis[12, 57] and that are influenced by Fe impurities in the electrolyte. The interaction with Fe impurities holds critical implications not just for intrinsic activity studies of perovskite nickelates, but for any investigation using electrocatalytic materials in alkaline electrolyzers, which generally do not use highly purified electrolytes and use stainless-steel components. This Fe-based effect cannot be ignored by transitioning from powder to epitaxial configurations, even if Ni redox waves cannot be seen in the voltammetry. The fact that nickelates with distinct structures, rhombohedral, oxygen-deficient particulate $LaNiO_3$, and tetragonal oxygen super-stoichiometric nanorod La_2NiO_4, are activated by Fe suggests these effects could be a universal phenomenon that has gone relatively unacknowledged. Interestingly, in this work this occurred in catalysts with full La-stoichiometry at the A-site while typically some substitution of the La at the A-site with an alkaline earth metal is required to observe instability in Co oxides[11, 12, 58, 59]. Another critical insight from this study is that in all of these samples the Ni redox waves are either absent or small (especially in spincoated thin films) and thus easy to miss within the initial cycles. In the case of epitaxial LNO films, *redox waves are completely absent*, but is still strongly activated by Fe in the electrolyte as we show in Figure 4c. In other words, there would be no clues that other Ni species are influencing catalysis while the activity was being measured.

Other studies have also reported pH-dependent OER catalytic activity for perovskite oxides in which activity decreases with pH. This observation, coupled with isotopic oxygen labelling and on-line electrochemical mass spectroscopy data showing oxygen exchange, has led to the proposal of a lattice oxygen evolution (LOER) mechanism.[60, 61] An alternate, proposal is that an oxidizing potential drives the reconstruction of the pristine material, a process which requires oxygen lability and exchange. The new surface species may be sensitive to soluble Fe, especially when the B-site is occupied by Ni or Co. Consequently, the decreasing activity with decreasing pH could be, at least in part, due to the corresponding decrease in soluble Fe by an order of magnitude with each unit decrease in pH, as has been suggested recently for $La_{1-x}Sr_xCoO_3$[12]. Since lattice oxygen exchange has been detected for NiO_xH_y,[62] it is still not clear whether LOER after reconstruction is from the perovskite or the *in-situ* formed NiO_xH_y.

Conclusion

Both $LaNiO_3$ and La_2NiO_4 exhibit a growth of redox-active Ni species that increases in quantity as a function of cycling and duration of chronoamperometric conditioning. Fe-spiking experiments demonstrate that high OER activity is achieved upon the introduction of Fe. After Fe introduction, further activity increase with cycle number correlates with the increased quantity of redox-active Ni. Measurements on epitaxial $LaNiO_3$ films show that Fe activation occurs on $LaNiO_3$ even when a clear pre-OER redox wave is not obviously present, because of low exposed catalyst surface area. Analysis of impedance spectroscopy, XPS and TEM data support the proposal that generation of redox-active surface species involves a structural transformation leading to increased electrochemically active surface area with cycling, a decrease in nominally surface O^{2-} content compared to -OH, and amorphization of the catalyst. Intrinsic OER activity represented by $TOF_{tm,redox}$ values calculated from the redox-active Ni available during the Fe spike experiments show that the redox-active species share similar characteristics despite disparate structures of the host $LaNiO_3$ and La_2NiO_4. La_2NiO_4 displays a higher tendency for the growth of redox-active Ni than $LaNiO_3$, indicating the significance of Ni-O termination in the formation of these surface species.

The data and analyses reported here show that interpretations of intrinsic activity and the correlation of this activity to electronic and structural features of the pristine material necessitate Fe-free conditions and pre- and post-mortem surface analysis. Reports of intrinsic activity of nickelate perovskites and related materials should be made with caution – especially if only a single voltammetry sweep or chronoamperometry is performed in unpurified electrolytes without paying close attention to precatalytic redox waves which may become prominent with further cycling. The implications of these results are that in any practical alkaline electrolyzer system (unpurified 30 wt% KOH and with stainless steel cell components) the activity of a perovskite nickelate catalyst will be controlled by its extent of surface reconstruction and interactions with Fe impurities. Future effort should focus on characterizing and tailoring the catalyst composition, along with the precise electrolye composition, to tune the activity and stability of this surface phase. The formation of these surface phases, their interaction with the underlying substrate, and catalytic turnover of intermediates, must fundamentally be related to nature of bonding within the material as well as adsorbates, and therefore its electronic structure. The use of descriptors from quantum mechanical calculations of electronic structure to understand structure-restructuring relationships in the presence of potential, water, and alkali electrolyte would thus be a valuable addition to the field of

heterogeneous OER electrocatalysis. Such approaches would complement typical calculations of intermediate binding energies[63].

Acknowledgements

S.B. gratefully acknowledges this work was supported by the National Science Foundation Chemical Catalysis Program, Award # 1955106. The ICP-MS instrument was funded by an NSF MRI Award #2117614. E.N. gratefully acknowledge the financial support from the United States Department of Energy (DOE), Basic Energy Science (BES), Chemical Sciences, Geosciences, and Biosciences Division, under award number DE-SC0020953/DE-SC0023645. Synthesis of $LaNiO_3$ epitaxial thin films was supported by the U.S. Department of Energy (DOE), Office of Science, Basic Energy Sciences, Division of Materials Sciences and Engineering, Synthesis and Processing Science Program, under Award #10122.

Method and materials

Synthesis. $LaNiO_3$ was prepared using a nitrate precipitation method. 1.95 mmol of nickel (II) nitrate hexahydrate and 2 mmol lanthanum (III) nitrate nonahydrate was weighed out and dissolved in 10 mL 18.2 MOhm nanopure water. A slight understoichiometry was chosen for the nickel nitrate to prevent minor NiO species formation. A mixed La/Ni hydroxide was precipitated by rapid addition of a 4 mL/4 mL mixture of water/semiconductor grade tetramethylammonium hydroxide. The resulting mixture was stirred for 30 minutes to ensure complete reaction. The solid was recovered with centrifugation, ground in an agate mortar and pestle for 5 minutes and calcined in air at 900°C for 12 h. The solid was ground and refired until a phase pure was obtained using powder X-ray diffraction. La_2NiO_4 rod synthesis was prepared using a reverse microemulsion procedure described in detail in prior work[37]. Epitaxial $LaNiO_3$ thin films with the thickness of 20 unit cells (~ 8 nm) were grown on (001) oriented $LaAlO_3$ substrates by using oxygen plasma–assisted molecular beam epitaxy (OPA-MBE). The growth details have been described elsewhere[45]

A reverse microemulsion based technique was used for the synthesis of rod-shaped La_2NiO_4 (214-LNO) nanostructures.[38, 64] A typical synthesis of 214-LNO involved the reaction between two quaternary phase microemulsions. Both the microemulsions contained equal amounts of cetyltrimethylammonium bromide (CTAB; 11.0 g), hexane (Sigma Aldrich, HPLC grade), and *n*-butanol (Sigma Aldrich >99%). The difference between the two microemulsions was that one of the microemulsions contained stoichiometric amounts of $La(NO_3)_3 \cdot 6H_2O$ (Sigma Aldrich, >99.999%) and $Ni(NO_3)_2 \cdot 6H_2O$ (Sigma Aldrich, >98%) salts (2 mmol equivalent) dissolved in 1.155 mL of deionized (DI) water (>18.2 MΩ). KOH solution was used in the anionic microemulsion to aid in precipitation of the hydroxides. The morphology of the samples can be changed by varying the ratio of water used to dissolve salts and that of CTAB. A water to CTAB ratio of 1.6 was used to obtain rod-shaped 214-LNO nanostructures. The two microemulsions were mixed and subsequently allowed to react for 4h to form a sol-gel mixture of metal

hydroxides. Subsequently, the formed hydroxides were collected by centrifugation, and washed thrice with ethanol and thrice with DI water. The precipitate was dried in an oven in air at 80°C overnight, followed by calcination in Ar at 835°C for 2h (heating rate: 2°C/min).

Electrochemical measurements. Catalyst films were either prepared by spincoating or by dropcasting onto Pt/Ti glass slides made using electron beam evaporation. Choice of coating technique is indicated for the given data in the text. Spincoated films were chosen for intrinsic activity measurements so that electron transport distances were reduced relative to dropcast films and conductive binder, which oxidizes during OER, could be excluded in ink preparation. Ink for spincoating was ~5:1 by mass of catalyst to Nafion binder in 2:1 by volume of isopropanol: nanopure water. Inks were sonicated for at least 1 hour before coating. A typical spincoating procedure involved adding ~80 uL onto the substrate after sonication and spinning at 3000 RPM for 2 minutes. Nafion was neutralized with a few drops of Fe-free 1 M KOH to avoid possible dissolution of the catalyst by reaction with acidic groups. All electrochemical measurements were performed in Fe/Ni free 1 M KOH (prepared from semiconductor-grade KOH using the standard method of Boettcher *et al.*[36]) using a Hg|HgO reference electrode calibrated against RHE and Pt coil counter electrode. Plastic cells were used and cleaned with 1 M sulfuric acid before experimentation to remove trace Fe from the cell. All electrochemistry was performed using a Biologic SP-300 potentiostat. Impedance spectroscopy was performed from 1 Hz to 7 MHz from the base voltage of 0.8 V vs Hg|HgO with 10 mV amplitude. The impedance data was fit to the equivalent circuit depicted as an inset in Figure 3b: a solution and cell resistance, R1, in series with a Randles cell element with constant phase element Q2 parallel with faradaic impedance, R2. A constant phase element was chosen because its impedance is similar to that of a pure capacitance, but more closely fit the slightly depressed semicircular shape of the measured impedance. Uncompensated series resistance (R_u) was extracted using impedance spectroscopy at 0 V vs Hg|HgO from 1 Hz to 1 MHz and was estimated from the associated Nyquist plot as the value of the real component of the impedance at 0 (or closest to 0) on the imaginary axis. All electrochemical data should be assumed to be iR_u-corrected unless otherwise indicated.

Characterization.

XRD studies were performed using a powder diffractometer (Bruker D2 Phaser) with a Cu Kα source. Scans were obtained between a 2θ of 20-80°. ICP-MS measurements (ThermoFisher iCAP-RQ) were performed in kinetic energy discrimination mode with calibrations of all measured elements having R^2 values > 0.998. All digestions of catalyst films were done with concentrated TraceMetal ® grade nitric acid (Fisher Scientific). Laboratory control standards containing known amounts of La, Ni, Fe, and Co were run at intervals between unknown samples to continually verify good performance of hardware and internal standards. X-ray photoelectron spectroscopy (XPS) studies done using an ESCALAB 250

(ThermoScientific). Spectra were obtained using an Al Kα monochromated (150 W, 20 eV pass energy, 500μm spot size) X-ray source. All samples were optimally charge-neutralized using an in-lens electron source combined with a low-energy Ar+ flood source. TEM data was acquired using a FEI 80-300kV (S)TEM equipped with a spherical aberration image corrector. All data was collected at 300kV. For IL-TEM experiments, a PELCO gold pinpointer grid (400 mesh, Ted Pella) was dipcoated by repeated rounds of immersion into the catalyst ink until a visible change of the grid color to that of the ink was achieved. Loading was not measured or controlled since only some locations with good contact between grid and catalyst were required for these studies. Powder x-ray diffractograms were obtained with a benchtop Bruker D2 Phaser

Acknowledgements

S.B. support by the National Science Foundation Chemical Catalysis Program, Award # 1955106 for this work. The ICP-MS instrument was funded by an NSF MRI Award #2117614. Y.O. acknowledges support from the China Scholars Council. E.N. gratefully acknowledge the financial support from the United States Department of Energy (DOE), Basic Energy Science (BES), Chemical Sciences, Geosciences, and Biosciences Division, under award number DE-SC0020953/DE-SC0023645. Synthesis of $LaNiO_3$ epitaxial thin films was supported by the U.S. Department of Energy (DOE), Office of Science, Basic Energy Sciences, Division of Materials Sciences and Engineering, Synthesis and Processing Science Program, under Award #1012

Author contributions

L.T. and S.B. conceived of the research with assistance from Y.O. S.W.B. directed the research project. L.T. collected most of the experimental data, with assistance from A.T. and K.D.; K.V. and S.S. directed by E.N. synthesized and characterized the R-P 214-LNO materials as well as advised on their properties. L. W. prepared the epitaxial $LaNiO_3$ films. L.T and S.W.B. analyzed the data and L.T. wrote the manuscript with contributions from S.B., E.N., K.V, S.S, and L.W.

Data availability

The data supporting the findings of this study are available from the authors upon request.

References

(1) Fabbri, E.; Schmidt, T. J. Oxygen Evolution Reaction—The Enigma in Water Electrolysis. *ACS Catal.* **2018**, *8* (10), 9765-9774. DOI: 10.1021/acscatal.8b02712 (acccessed 2022-05-16T00:40:52).

(2) Bockris, J. O. M.; Otagawa, T. Mechanism of oxygen evolution on perovskites. J. Phys. Chem.: 1983; Vol. 87, pp 2960 - 2971.

(3) Song, J. e. a. Synergistic role of E_g filling and anion-cation hybridization in enhancing the oxygen evolution reaction activity in nickelates. *ACS Appl. Energy Mater.* **2021**.
(4) Giordano, L.; Akkiraju, K.; Jacobs, R.; Vivona, D.; Morgan, D.; Shao-Horn, Y. Electronic Structure-Based Descriptors for Oxide Properties and Functions. *Acc. Chem. Res.* **2022**, *55* (3), 298-308.

(5) Suntivich, J.; May, K. J.; Gasteiger, H. A.; Goodenough, J. B.; Shao-Horn, Y. A perovskite oxide optimized for oxygen evolution catalysis from molecular orbital principles. Science: 2011; Vol. 334, pp 1383-1385.

(6) Hammer, B.; Nørskov, J. K. Electronic factors determining the reactivity of metal surfaces. *Surf. Sci.* **1995**, *343* (3), 211-220.

(7) Hammer, B.; Norskov, J. K. Why gold is the noblest of all the metals. *Nature* **1995**, *376* (6537), 238-240.

(8) Hammer, B.; Nørskov, J. K. Theoretical surface science and catalysis—calculations and concepts. In *Advances in Catalysis*, Vol. 45; Academic Press, 2000; pp 71-129.

(9) Fabbri, E.; et al. Dynamic surface self-reconstruction is the key of highly active perovskite nano-electrocatalysts for water splitting. Nature Materials: 2017; Vol. 16.

(10) Burke, M. S.; Kast, M. G.; Trotochaud, L.; Smith, A. M.; Boettcher, S. W. Cobalt–Iron (Oxy)hydroxide Oxygen Evolution Electrocatalysts: The Role of Structure and Composition on Activity, Stability, and Mechanism. *J. Am. Chem. Soc.* **2015**, *137* (10), 3638-3648.

(11) Shen, T.-H. e. a. Oxygen evolution reaction in $Ba_{0.5}Sr_{0.5}Co_{0.8}Fe_{0.2}O_{3-y}$ aided by intrinsic Co/Fe spinel-like surface. *J. Am. Chem. Soc.* **2020**.

(12) Lopes, P. P. e. a. Dynamically stable active sites from surface evolution of perovskite materials during the oxygen evolution reaction. *J. Am. Chem. Soc.* **2021**.

(13) Boucly, A. e. a. Surface segregation acts as surface engineering for the oxygen evolution reaction on perovskite oxides in alkaline media. *Chem. Mater.* **2020**, *32*, 5256-5263.

(14) Boucly, A.; Artiglia, L.; Fabbri, E.; Palagin, D.; Aegerter, D.; Pergolesi, D.; Novotny, Z.; Comini, N.; Diulus, J. T.; Huthwelker, T.; et al. Direct evidence of cobalt oxyhydroxide formation on a $La_{0.2}Sr_{0.8}CoO_3$ perovskite water splitting catalyst. *J. Mater. Chem. A* **2022**, *10* (5), 2434-2444,

(15) Wiegmann, T.; Pacheco, I.; Reikowski, F.; Stettner, J.; Qiu, C.; Bouvier, M.; Bertram, M.; Faisal, F.; Brummel, O.; Libuda, J.; et al. Operando Identification of the Reversible Skin Layer on Co_3O_4 as a Three-Dimensional Reaction Zone for Oxygen Evolution. *ACS Catal.* **2022**, *12* (6), 3256-3268.

(16) Zhang, T.; Nellist, M. R.; Enman, L. J.; Xiang, J.; Boettcher, S. W. Modes of Fe Incorporation in Co–Fe (Oxy)hydroxide Oxygen Evolution Electrocatalysts. *ChemSusChem* **2019**, *12* (9), 2015-2021,

(17) Burke, M. S.; Zou, S.; Enman, L. J.; Kellon, J. E.; Gabor, C. A.; Pledger, E.; Boettcher, S. W. Revised Oxygen Evolution Reaction Activity Trends for First-Row Transition-Metal (Oxy)hydroxides in Alkaline Media. *J. Phys. Chem. Lett.* **2015**, *6* (18), 3737-3742.

(18) Binninger, T. Thermodynamic explanation of the universal correlation between oxygen evolution activity and corrosion of oxide catalysts. *Nat. Sci. Rep.* **2015**.

(19) Trotochaud, L.; Ranney, J. K.; Williams, K. N.; Boettcher, S. W. Solution-cast metal oxide thin film electrocatalysts for oxygen evolution. **2012**, *134*, 17253-17261.

(20) Trotochaud, L.; Young, S. L.; Ranney, J. K.; Boettcher, S. W. Nickel-iron oxyhydroxide oxygen-evolution electrocatalysts: The role of intentional and incidental iron incorporation. **2014**, *136*, 6744-6753.

(21) Corrigan, D. A. The catalysis of the oxygen evolution reaction by iron impurities in thin film nickel oxide electrodes. **1987**, *134*, 377.

(22) Sunding, M. F. e. a. XPS characterization of in-situ treated lanthanum oxide and hydroxide using tailored charge referencing and peak fitting procedures. *J. Electron Spectrosc. Relat. Phenom.* **2011**, *184*, 399-409.

(23) Biesinger, M. C. e. a. Resolving surface chemical states in XPS analysis of first row transition metals, oxides and hydroxides: Cr, Mn, Fe, Co, Ni. *Appl. Surf. Sci.* **2011**, *257*, 2717-2730.

(24) San Choi, J.; Ahn, C. W.; Bae, J.-S.; Kim, T. H. Identifying a perovskite phase in rare-earth nickelates using X-ray photoelectron spectroscopy. *Current Applied Physics* **2020**, *20* (1), 102-105.

(25) Payne, B. P.; Biesinger, M. C.; McIntyre, N. S. Use of oxygen/nickel ratios in the XPS characterisation of oxide phases on nickel metal and nickel alloy surfaces. *J. Electron Spectrosc. Relat. Phenom.* **2012**, *185* (5), 159-166.

(26) Biesinger, M. C.; Payne, B. P.; Lau, L. W. M.; Gerson, A.; Smart, R. S. C. X-ray photoelectron spectroscopic chemical state quantification of mixed nickel metal, oxide and hydroxide systems. *Surf. Interface Anal.* **2009**, *41* (4), 324-332.

(27) Krivina, R. A.; Lindquist, G. A.; Yang, M. C.; Cook, A. K.; Hendon, C. H.; Motz, A. R.; Capuano, C.; Ayers, K. E.; Hutchison, J. E.; Boettcher, S. W. Three-Electrode Study of Electrochemical Ionomer Degradation Relevant to Anion-Exchange-Membrane Water Electrolyzers. *ACS Appl. Mater. Interfaces* **2022**, *14* (16), 18261-18274.

(28) Batchellor, A. S.; Boettcher, S. W. Pulse-electrodeposited Ni-Fe (oxy)hydroxide oxygen evolution electrocatalysts with high geometric and intrinsic activities at large mass loadings. *ACS Catal.* **2015**, *5* (11), 6680-6689.

(29) Stevens, M. B.; Trang, C. D. M.; Enman, L. J.; Deng, J.; Boettcher, S. W. Reactive Fe-sites in Ni/Fe (Oxy)hydroxide are responsible for exceptional oxygen electrocatalysis activity. *J. Am. Chem. Soc.*: 2017; Vol. 139, pp 11361-11364.

(30) Ou, Y.; Twight, L.; Samanta, B.; *al., e.* Cooperative Fe Sites on Transition Metal (Oxy)hydroxides for High Oxygen Evolution Activity. ChemRxiv. Cambridge. *Chem. Rxiv.* **2023**.

(31) Sun, Y.; Wang, J.; Xi, S.; Shen, J.; Luo, S.; Ge, J.; Sun, S.; Chen, Y.; Hanna, J. V.; Li, S.; et al. Navigating surface reconstruction of spinel oxides for electrochemical water oxidation. *Nat. Commun.* **2023**, *14* (1), 2467.

(32) Grimaud, A.; Diaz-Morales, O.; Han, B.; Hong, W. T.; Lee, Y.-L.; Giordano, L.; Stoerzinger, K. A.; Koper, M. T. M.; Shao-Horn, Y. Activating lattice oxygen redox reactions in metal oxides to catalyse oxygen evolution. Nat. Chem.: 2017; Vol. 9, pp 457-465.
(33) Samira, S.; Gu, X.-K.; Nikolla, E. Design Strategies for Efficient Nonstoichiometric Mixed Metal Oxide Electrocatalysts: Correlating Measurable Oxide Properties to Electrocatalytic Performance. *ACS Catal.* **2019**, *9* (11), 10575-10586.

(34) Rumble, J. R.; Rumble, J. C. H. o. C. a. P., 98th Edition; Physics, C. H. o. C. a.; CRC Press LLC. *CRC Handbook of Chemistry and Physics, 103rd Edition*; CRC Press LLC, 2021.
(35) Cornell, R. M.; Schwertmann, U. *The Iron Oxides: Structure, Properties, Reactions, Occurrences, and Uses, 2nd Edition*; Wiley-VCH, 2003.

(36) Liu, L.; Twight, L. P.; Fehrs, J. L.; Ou, Y.; Sun, D.; Boettcher, S. W. Purification of Residual Ni and Co Hydroxides from Fe-Free Alkaline Electrolyte for Electrocatalysis Studies. *ChemElectroChem* **2022**, *9* (15)

(37) Ma, X.; Wang, B.; Xhafa, E.; Sun, K.; Nikolla, E. Synthesis of shape-controlled La2NiO4+δ nanostructures and their anisotropic properties for oxygen diffusion. *Chem. Commun.* **2015**, *51* (1), 137-140.

(38) Gu, X.-K.; Carneiro, J. S. A.; Samira, S.; Das, A.; Ariyasingha, N. M.; Nikolla, E. Efficient Oxygen Electrocatalysis by Nanostructured Mixed-Metal Oxides. *J. Am. Chem. Soc.* **2018**, *140* (26), 8128-8137.
(39) Ma, X.; Carneiro, J. S. A.; Gu, X.-K.; Qin, H.; Xin, H.; Sun, K.; Nikolla, E. Engineering Complex, Layered Metal Oxides: High-Performance Nickelate Oxide Nanostructures for Oxygen Exchange and Reduction. *ACS Catal.* **2015**, *5* (7), 4013-4019.

(40) Petrie, J. R.; Cooper, V. R.; Freeland, J. W.; Meyer, T. L.; Zhang, Z.; Lutterman, D. A.; Lee, H. N. Enhanced Bifunctional Oxygen Catalysis in Strained LaNiO3 Perovskites. *J. Am. Chem. Soc.* **2016**, *138* (8), 2488-2491.

(41) Gu, X.-K.; Samira, S.; Nikolla, E. Oxygen Sponges for Electrocatalysis: Oxygen Reduction/Evolution on Nonstoichiometric, Mixed Metal Oxides. *Chem. Mater.* **2018**, *30* (9), 2860-2872.

(42) Samira, S. e. a. Dynamic surface reconstruction unifies the electrocatalytic oxygen evolution performance of nonstoichiometric mixed metal oxides. *JACS Au* **2021**.

(43) Forslund, R. P.; Hardin, W. G.; Rong, X.; Abakumov, A. M.; Filimonov, D.; Alexander, C. T.; Mefford, J. T.; Iyer, H.; Kolpak, A. M.; Johnston, K. P.; et al. Exceptional electrocatalytic oxygen evolution via tunable charge transfer interactions in $La_{0.5}Sr_{1.5}Ni_{1-x}Fe_xO_{4\pm\delta}$ Ruddlesden-Popper oxides. *Nat. Commun.* **2018**, *9* (1), 3150.

(44) Friebel, D.; Louie, M. W.; Bajdich, M.; Sanwald, K. E.; Cai, Y.; Wise, A. M.; Cheng, M.-J.; Sokaras, D.; Weng, T.-C.; Alonso-Mori, R.; et al. Identification of Highly Active Fe Sites in (Ni,Fe)OOH for Electrocatalytic Water Splitting. *J. Am. Chem. Soc.* **2015**, *137* (3), 1305-1313.

(45) Liu, J.; Jia, E.; Wang, L.; Stoerzinger, K. A.; Zhou, H.; Tang, C. S.; Yin, X.; He, X.; Bousquet, E.; Bowden, M. E.; et al. Tuning the Electronic Structure of LaNiO3 through Alloying with Strontium to Enhance Oxygen Evolution Activity. *Advanced Science* **2019**, *6* (19), 1901073,

(46) Sankannavar, R. e. a. Impact of strontium-substitution on oxygen evolution reaction of lanthanum nickelates in alkaline solution. *J. Electrochem. Soc* **2018**, *165*.

(47) Wang, L.; Adiga, P.; Zhao, J.; Samarakoon, W. S.; Stoerzinger, K. A.; Spurgeon, S. R.; Matthews, B. E.; Bowden, M. E.; Sushko, P. V.; Kaspar, T. C.; et al. Understanding the Electronic Structure Evolution of Epitaxial LaNi1–xFexO3 Thin Films for Water Oxidation. *Nano Lett.* **2021**, *21* (19), 8324-8331.

(48) Baeumer, C. e. a. Tuning electrochemically driven surface transformations in atomically flat $LaNiO_3$ thin films for water electrolysis. *Nat. Mater.* **2021**.

(49) Liu, J. e. a. Dynamic lattice oxygen participation on perovskite $LaNiO_3$ during oxygen evolution reaction. *J. Phys. Chem. C.* **2020**, *124*, 15386-15390.

(50) Bak, J.; Bin Bae, H.; Chung, S.-Y. Atomic-scale perturbation of oxygen octahedra via surface ion exchange in perovskite nickelates boosts water oxidation. *Nat. Commun.* **2019**, *10* (1), 2713.

(51) Adiga, P.; Wang, L.; Wong, C.; Matthews, B. E.; Bowden, M. E.; Spurgeon, S. R.; Sterbinsky, G. E.; Blum, M.; Choi, M.-J.; Tao, J.; et al. Correlation between oxygen evolution reaction activity and surface compositional evolution in epitaxial $La_{0.5}Sr_{0.5}Ni_{1-x}Fe_xO_{3-\delta}$ thin films. *Nanoscale* **2023**, *15* (3), 1119-1127.

(52) Corrigan, D. A. The Catalysis of the Oxygen Evolution Reaction by Iron Impurities in Thin Film Nickel Oxide Electrodes. *J. Electrochem. Soc.* **1987**, *134* (2), 377-384.

(53) Chung, D. Y.; Lopes, P. P.; Farinazzo Bergamo Dias Martins, P.; He, H.; Kawaguchi, T.; Zapol, P.; You, H.; Tripkovic, D.; Strmcnik, D.; Zhu, Y.; et al. Dynamic stability of active sites in hydr(oxy)oxides for the oxygen evolution reaction. *Nat. Energy.* **2020**, *5* (3), 222-230.

(54) Son, Y. J.; Kim, S.; Leung, V.; Kawashima, K.; Noh, J.; Kim, K.; Marquez, R. A.; Carrasco-Jaim, O. A.; Smith, L. A.; Celio, H.; et al. Effects of Electrochemical Conditioning on Nickel-Based Oxygen Evolution Electrocatalysts. *ACS Catal.* **2022**, *12* (16), 10384-10399.

(55) Wygant, B. R.; Kawashima, K.; Mullins, C. B. Catalyst or Precatalyst? The Effect of Oxidation on Transition Metal Carbide, Pnictide, and Chalcogenide Oxygen Evolution Catalysts. *ACS Energy Lett.* **2018**, *3* (12), 2956-2966.

(56) Gong, L.; Chng, X. Y. E.; Du, Y.; Xi, S.; Yeo, B. S. Enhanced Catalysis of the Electrochemical Oxygen Evolution Reaction by Iron(III) Ions Adsorbed on Amorphous Cobalt Oxide. *ACS Catal.* **2018**, *8* (2), 807-814.

(57) Yagi, S.; et al. Covalency-reinforced oxygen evolution reaction catalyst. Nat. Comm.: 2015; Vol. **6**, p 8249.

(58) Risch, M.; Grimaud, A.; May, K. J.; Stoerzinger, K. A.; Chen, T. J.; Mansour, A. N.; Shao-Horn, Y. Structural changes of cobalt-based perovskites upon water oxidation investigate by EXAFS. J. Phys. Chem. C.: 2013; Vol. 117, pp 8628 - 8635.

(59) May, K. J.; Carlton, C. E.; Stoerzinger, K. A.; Risch, M.; Suntivich, J.; Lee, Y.-L.; Grimaud, A.; Shao-Horn, Y. Influence of oxygen evolution during water oxidation on the surface of perovskite oxide catalysts. J. Phys. Chem. Lett.: 2012; Vol. 3, pp 3264-3270.

(60) Grimaud, A.; May, K. J.; Carlton, C. E.; Lee, Y.-L.; Risch, M.; Hong, W. T.; Zhou, J.; Shao-Horn, Y. Double perovskites as a family of highly active catalysts for oxygen evolution in alkaline solution. *Nature Communications*: 2013; Vol. 4, p 2439.
(61) Liu, J.; Jia, E.; Stoerzinger, K. A.; Wang, L.; Wang, Y.; Yang, Z.; Shen, D.; Engelhard, M. H.; Bowden, M. E.; Zhu, Z.; et al. Dynamic Lattice Oxygen Participation on Perovskite LaNiO3 during Oxygen Evolution Reaction. *J. Phys. Chem. C* **2020**, *124* (28), 15386-15390.

(62) He, Z.; Zhang, J.; Gong, Z.; Lei, H.; Zhou, D.; Zhang, N.; Mai, W.; Zhao, S.; Chen, Y. Activating lattice oxygen in NiFe-based (oxy)hydroxide for water electrolysis. *Nat. Commun.* **2022**, *13* (1), 2191.

(63) Man, I. C.; et al. Universality in oxygen evolution electrocatalysis on oxide surfaces. *ChemCatChem*: 2011; Vol. 3, pp 1159-1165.

(64) Carneiro, J. S. A.; Williams, J.; Gryko, A.; Herrera, L. P.; Nikolla, E. Embracing the Complexity of Catalytic Structures: A Viewpoint on the Synthesis of Nonstoichiometric Mixed Metal Oxides for Catalysis. *ACS Catal.* **2020**, *10* (1), 516-527. DOI: